Journal of Nuclear Materials 506 (2018) 83–91

Contents lists available at ScienceDirect

Journal of Nuclear Materials

journal homepage: www.elsevier.com/locate/jnucmat

Fatigue properties of tungsten from two different processing routes

Jemila Habainy [a, b, *], Andreas Lövberg [b], Srinivasan Iyengar [a, b], Yongjoong Lee [a], Yong Dai [c]

[a] European Spallation Source ESS ERIC, Box 176, 22100 Lund, Sweden
[b] Division of Materials Engineering, Lund University, Box 118, 22100 Lund, Sweden
[c] Paul Scherrer Institut, 5232 Villigen PSI, Switzerland

ARTICLE INFO

Article history:
Received 29 November 2016
Received in revised form
28 July 2017
Accepted 26 October 2017
Available online 31 October 2017

Keywords:
Fatigue limit
Tungsten
Spallation material

ABSTRACT

Fatigue failure is a distinct possibility in spallation targets like tungsten, subjected to cyclic thermo-mechanical loading caused by beam trips and beam pulses. In this study, the tensile and fatigue properties of pure tungsten from two different processing routes have been determined at room temperature. The specimens tested were sintered, rolled and annealed (RA), as well as sintered and HIPed tungsten (SH).

Tensile tests showed low total strain (~0.25%) and negligible plastic strain for both specimens. However, the UTS for rolled specimens (~1 GPa) was much higher relative to the HIPed material (567 MPa).

As tungsten is very brittle, fatigue testing was done primarily under stress-control, using the staircase method and a near zero stress ratio. For the rolled and HIPed materials, fatigue limits (no specimen failure up to $2 \cdot 10^6$ load cycles) were determined to be 350 MPa and 180 MPa, respectively. In addition, results from strain-controlled multiple-step testing (strain ratio ~0) indicated a slight relaxation in stress for the HIPed material while the rolled specimens showed a purely elastic response.

The implication of fatigue test results for spallation target design is discussed.

1. Introduction

The European Spallation Source (ESS) facility is currently under construction in Lund and scheduled to deliver its first neutrons by 2019. The neutrons are produced through a spallation process where the target material is subjected to a high energy and high power, pulsed proton beam. The pulse frequency is 14 Hz with a duration of 2.86 ms. The energy and power levels are 2 GeV and 5 MW, respectively, and each pulse deposits 357 kJ in the target. The target is designed as a 36-sector wheel, rotating in sync with the beam pulse. Each sector consists of $8 \times 3 \times 1$ cm^3 sized blocks of tungsten, separated by helium cooling channels.

The choice of pure tungsten as the spallation material offers a large total neutron yield due to its high atomic weight and density. Other attractive properties of tungsten are the high melting point (~3400 °C) and good thermal conductivity. However, the brittle nature of tungsten and a ductile-to-brittle transition temperature (DBTT) that is well above room temperature puts the structural integrity of the target at risk.

Cyclic thermo-mechanical loading caused by beam trips and beam pulses can drive the temperatures in the tungsten blocks momentarily up to a maximum of 500 °C. Stresses due to beam pulse induced temperature changes are calculated to be in the range of 44–110 MPa, giving a maximum stress amplitude of 33 MPa [1]. The loss of structural integrity due to thermal cycling may lead to a non-optimal cooling flow configuration, which would create a hot spot in the target. An increase of the temperature in the tungsten will lead to a higher rate of diffusion driven release of radioactive isotopes.

Any dust produced during vibrations of the target wheel will be filtered and will not lead to a cooling channel blockage. Furthermore, experiments dedicated to assessing the dust production rate, using a vibrating test stand with tungsten blocks in steel cassettes, show that the dust collected after the experiment only contains steel from the cassettes [2].

The lifetime of the target is estimated to be about 5 years, which corresponds to approximately $4 \cdot 10^7$ pulses and $2 \cdot 10^6$ beam trips per each target segment [3]. The fatigue life of tungsten strongly depends on the quality of the material, as well as the processing and surface conditions. A good understanding of the effect of these factors on the fatigue properties of pure tungsten is therefore

* Corresponding author. European Spallation Source ESS ERIC, Box 176, 22100 Lund, Sweden.
E-mail address: jemila.habainy@esss.se (J. Habainy).

https://doi.org/10.1016/j.jnucmat.2017.10.061
0022-3115/

essential while designing the target.

1.1. Previous studies

An extensive review of the available literature on fatigue in tungsten was made in conjunction with a recently published article on the fatigue properties of pure tungsten at different temperatures [4]. It shows that there are very few studies on stress-controlled fatigue testing of pure tungsten. Many papers focus on the mechanical properties of tungsten [5–8], some on the effects of alloying additions [9,10], and others on the causes of the DBTT shift [11–13]. The only other study on the fatigue properties of tungsten was published in 1981. Schmunk and Korth [14] used cross-rolled tungsten in both as-received and recrystallized condition to test the tensile and low-cycle fatigue properties at room temperature and at 815 °C. Data for the recrystallized tungsten showed a relatively lower fatigue limit at both temperatures. The room temperature tests had to be carried out under load control, due to negligible plasticity. The high temperature tests could however be performed under strain control.

The room temperature tests in Habainy et al. [4] showed that the fatigue limits of tungsten in the rolled condition were higher (however with large scatter) than those for the forged specimens. The orientation of the rolled specimens was shown to be significant and the fatigue limit corresponding to $2 \cdot 10^6$ cycles was observed to be ~237 MPa in the rolling direction as compared to ~137 MPa in the transverse direction. The forged specimens had a minimum fatigue limit of ~125 MPa.

Gludovatz et al. [15] showed that size and shape of the grains, as well as the degree of deformation and dislocation density, have a greater impact on the fracture behavior of tungsten, than grain boundary impurities. HIPed material in their study had a higher grain boundary dislocation density due to the elongated grain structure, which seems to have outweighed the negative effect on fracture toughness caused by the grain boundary impurities found in the sintered material.

2. Materials and methods

In the present study, tungsten specimens in the sintered, rolled and annealed (RA) as well as sintered and HIPed (SH) conditions have been used. The RA specimens were oriented along the rolling direction. All the specimens were supplied by PLANSEE Metall GmbH, Austria.

The DBTT for tungsten is relatively high, reportedly starting from 250° for hot rolled tungsten and about 350 °C for hot forged [16]. Gorynin et al. [17] have reported that the irradiation of tungsten to a damage level around 0.1 dpa pushes the DBTT to above 500 °C, which is close to the operating temperature of the ESS target. Damage levels in the target are estimated to reach 2 dpa per year, meaning that a newly commissioned target would become brittle already after a month of operation. It was therefore decided to carry out fatigue testing in this work at room temperature, in the brittle regime of tungsten.

The specimens used in this study are tested in the as-received condition. The impurity content is shown in Table 1. The specimen geometry, which is the same for both tensile and fatigue tests, is shown in Fig. 1. According to specifications from the supplier the surface roughness in the gauge section is below 1.6 μm. Prior to testing, each specimen was examined using an optical microscope. All surface defects and their positions, including machining stripes and marks from damage during handling, were noted. The microstructure was examined after a polishing procedure followed by etching with Murakami's reagent, in accordance with ASTM E407 [18]. The average grain size of the material was measured using the intercept method described in ASTM E112-13 [19]. Lines of equal length are randomly drawn over the micrograph, and the average number of grain boundary intercepts gives an estimation of the grain size.

Table 1
Impurity elements in tungsten.[a]

Element	Typical max. value [*ppm*]	Guaranteed max. value [*ppm*]
Al	1	15
Cr	3	20
Cu	1	10
Fe	8	30
K	1	10
Mo	12	100
Ni	2	20
Si	1	20
C	6	30
H	0	5
N	1	5
O	2	20
Cd	1	5
Hg	0	1
Pb	1	5

[a] PLANSEE Metall GmbH, Austria.

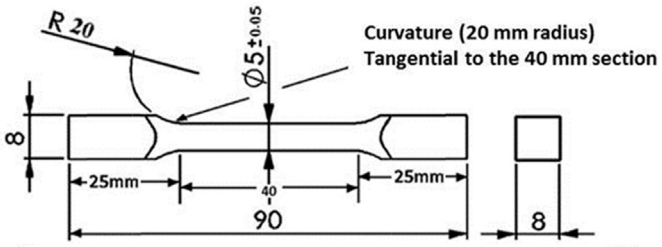

Fig. 1. Specimen geometry.

2.1. Tensile and fatigue testing

The tensile and fatigue tests were carried out in a MTS servo-hydraulic load frame with a maximum capacity of 250 kN, using an Instron 8500 control system. The tensile tests were carried out in accordance with the ASTM E8M standard [20] for testing metallic materials. According to ASTM E8M, for materials with an expected elongation of less than 5%, the strain rate should be set at 0.015 ± 0.006 mm/mm/min. Taking into account the gauge length of the specimen, an elongation rate of 0.6 mm/min has been used in this study.

Due to the brittleness and low plasticity exhibited by tungsten at room temperature, fatigue testing was carried out primarily under stress-control. In these tests only tensile stresses were applied ($S_{min} = 5$ MPa, for all tests). This provides a more conservative estimate of the fatigue limit, as cracks generally do not propagate during compressive loading. However, crack growth can still occur during loading in compression if residual tensile stresses are present [21].

Since the brittle nature of the specimens eliminates any significant difference in true vs. engineering stress-strain, all tensile and fatigue data in this paper are presented in the latter form.

At ESS the frequency of the pulsed beam will be 14 Hz. As the target is rotating, and is divided into 36 sectors, the resulting thermo-mechanical load on each section will occur at a 14/36 = 0.39 Hz. Running a test of $2 \cdot 10^6$ cycles would require more than 1400 h, in order to reduce the time a higher frequency of 25 Hz was chosen for all the stress-controlled fatigue tests in this work.

The staircase method (also known as the up-and-down method) [22] was chosen for determining the fatigue limit and its statistical variations. Specimens surviving $2{\cdot}10^6$ cycles without failure were considered runouts. This limit corresponds to the estimated number of beam trips during the suggested lifetime of the target. The staircase method uses a simple procedure in which a specimen is tested at a given starting stress until failure or runout. If the specimen fails at a given stress amplitude the stress level for the next specimen is decreased. If there is a run out ($2{\cdot}10^6$ cycles) the stress level is instead increased [23]. The results from the staircase testing are analyzed using the maximum likelihood estimation (MLE), assuming a normal distribution of the threshold stress. It is generally agreed that MLE provides a good estimate of the mean fatigue limit. It was previously thought that the staircase method required a large sample size (40–50 specimens or more). However, Brownlee et al. [24] have shown that the method is fairly reliable for sample sizes as small as 5 to10, and this is widely recognized in literature. According to common practice, the initial stress level should be set at 35–50% of the UTS [25].

The deformation response of tungsten in the low cycle fatigue (LCF) regime was studied by strain-controlled testing using the multiple-step method. Each step included 50 cycles with a fully reversed or a negative strain ratio. In view of the limited number of specimens available for fatigue testing, this method was useful for getting data over a range of strains. The multiple-step method is schematically shown in Fig. 2. LCF testing was done at a constant frequency of 1 Hz and a maximum of 10^4 cycles ($2{\cdot}10^4$ reversals). The cyclic variation in strain followed a saw-tooth waveform, which was generated using Instron Waverunner software.

3. Results and discussion

3.1. Surface condition

The surface condition of both types of tungsten was observed to be reasonably good, with only a few shallow machining stripes or other surface defects being visible. SH materials were noted to be generally more porous, making it difficult to get a very smooth surface on these specimens. Typical surfaces in the gauge section of SH and RA tungsten specimens are shown in Fig. 3.

3.1.1. Pore morphology

The distribution of pores in a material subjected to mechanical loading is important since pore clusters (near or at the surface) can act as stress concentration sites for the initiation of fatigue cracks. Pores would also lower the effective load-bearing area resulting in a lower tensile strength. The shape of the pores is also an important factor which affects fatigue life - an irregular shape is more detrimental than a perfectly round shape.

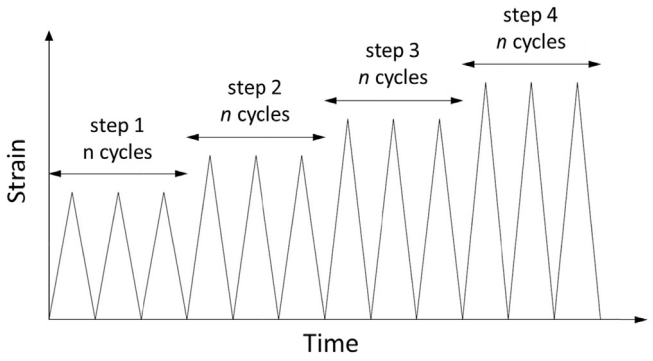

Fig. 2. Multiple-step strain-controlled fatigue testing.

The pore shape can be characterized using a form factor f_{shape} [26,27] which is defined as:

$$f_{shape} = 4\pi A/P^2 \quad (1)$$

where 'A' and 'P' represent the area and perimeter of the pore. A value of unity for the form factor corresponds to a completely rounded pore. Using the image processing software ImageJ to analyze the micrographs, the variation of shape factor with pore size was studied. Fig. 4 shows the relationship for the SH specimen, with about 4.3% porosity. As seen in the figure, smaller pores tend to be spherical, large pores are irregular probably due to a combination of several smaller pores. Only pores larger than 0.7 μm^2 were quantified in order to avoid bias resulting from resolution where very small pores are only a few pixels in size. At the resolution used here, 1 μm corresponds to approximately 9–10 pixels.

3.2. Microstructure

Fig. 5a shows the microstructure of a SH tungsten specimen. It is seen that the pores (the black dots in the image) are uniformly distributed in the microstructure. Fig. 14 in the fractography section of this paper also illustrates the pore distribution in the SH material. The variation in grain size is shown in Fig. 5b. The size is in the range 10–85 μm, with an average around 30 μm.

The RA specimen has very large, thin and interlocking grains, some as long as 1000 μm. These grains are clearly visible to the naked eye after polishing and etching. The surface image shown in Fig. 6a was obtained after etching with Murakami's reagent for over 200s and reveals details within the large grains which indicate a subgrain structure. Fig. 6b shows the effect of rolling using a triplanar micrograph. The top view of this micrograph shows the rolling plane. In the literature, subgrain structure of rolled tungsten has been observed by Gludovatz et al. [28], Briant et al. [29], as well as Rieth et al. [30].

3.3. Density

The densities of four SH and four RA specimens were determined using the Archimedes Buoyancy method. The average porosity was estimated by comparing the results to the reported density of pure tungsten at 20 °C, which is 19.3 g/cm^3 [31]. The average density and porosity of SH and RA tungsten are presented in Table 2. As expected, RA tungsten is significantly denser than SH, and the value for the SH specimen is in good agreement with the reported porosity of 4% for HIPed tungsten [15]. A minimum density of 19.0 g/cm^3 has been specified for the tungsten bricks in the spallation target. This would correspond to a maximum porosity of 1.55%.

3.4. Hardness

Microhardness measurements were performed using a load of 400 g and a dwell time of 15s. The results showed that the RA tungsten specimens were relatively harder, with an average Vickers hardness number of 508 VHN. The corresponding value for the SH specimens was determined to be 389 VHN. However, it may be noted that the pores are fine and well distributed in SH specimens, which makes it difficult to obtain indentations not affected by the pores.

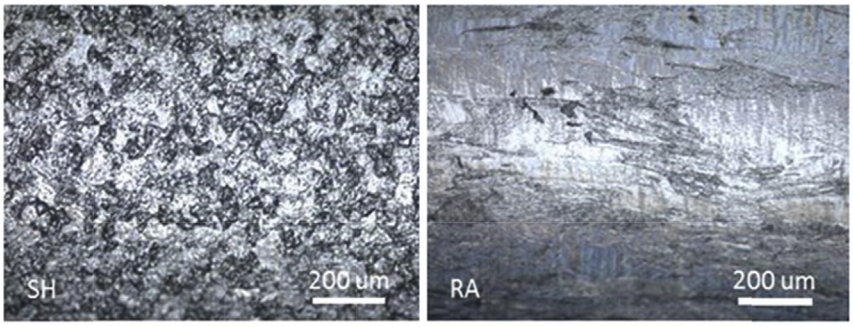

Fig. 3. Images of typical specimen surfaces (SH: sintered and HIPed, RA: sintered, rolled, and annealed).

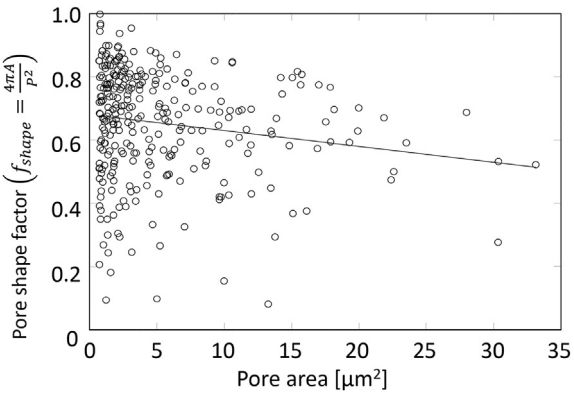

Fig. 4. Pore shape vs pore size in the SH specimens.

3.5. Tensile tests

Engineering stress-strain diagrams corresponding to the monotonic tensile response shown by two SH and one RA specimens are presented in Fig. 7. The experimental data are summarized in Table 3. It is seen that both types of specimens display negligible plasticity. The average ultimate tensile strength of the SH specimens is around 40% lower relative to the RA specimen. The SH specimens also display lower Young's modulus values, which can be explained by the higher porosity of the materials [32].

3.6. Stress-controlled fatigue testing

Fatigue data from constant stress amplitude tests are usually presented in a Wöhler plot where the stress amplitude S_a, for fully reversed loading, is plotted against the number of cycles to failure (N_f). In this work, all the tests have been carried out in the tensile regime with the minimum stress at 5 MPa.

The first SH fatigue specimen, SH4, was tested at an initial stress

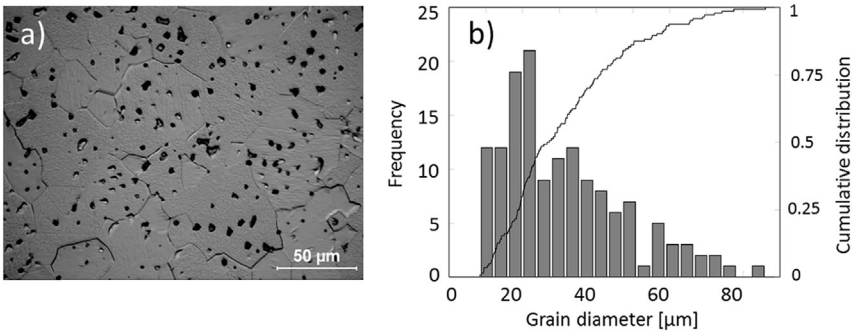

Fig. 5. a) Microstructure and b) grain size distribution in the SH specimen.

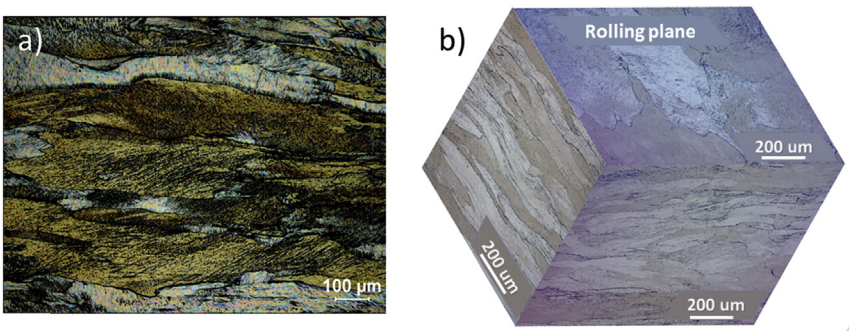

Fig. 6. Optical image of the RA specimen a) surface perpendicular to the rolling direction, b) Triplanar micrograph, showing the rolling plane.

Table 2
Average density at 20 °C.

Specimen	Density [g/cm^3]	Porosity [%]
SH	18.475	4.28
RA	19.208	0.48

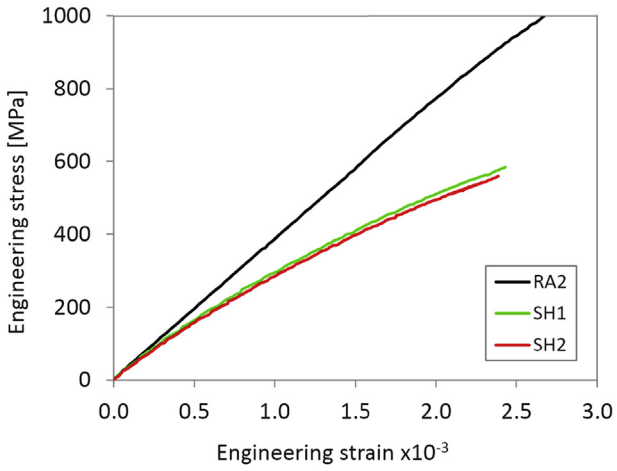

Fig. 7. Tensile testing of SH and RA specimens at room temperature.

Table 3
Tensile test data at room temperature.

Property	SH1	SH2	RA2
Young's Modulus [GPa]	323	332	393
UTS [MPa]	560	573	998
Porosity [%]	4.21	4.37	0.92

amplitude of 180 MPa and resulted in a runout. The stress amplitude was then ramped up in several steps until the specimen failed at 250 MPa. This was done in order to determine the fatigue strength using the least number of specimens. A similar approach was adopted for RA specimens. Data for the runout specimen SH4 at 180 MPa were used in staircase testing between the data for specimens SH9 and SH10. The last fatigue specimen, SH19, was used to get an additional data point in the higher stress regime. A few of the RA runouts were tested again at higher stress amplitudes. These results are not included in the staircase testing and the data is not used for determining the fatigue limit. The results serve only as an indication of the fatigue behavior at higher stresses. Fig. 8 shows S-N data for SH as well as RA specimens. The data from staircase testing are summarized in Table 4.

The Basquin equation [33] for the high cycle, low strain regime can be expressed as:

$$S_a = \text{Stress Amplitude} = \Delta S/2 = S_f'\left(2N_f\right)^b \quad (2)$$

where S_f' and 'b' are the fatigue strength coefficient and exponent, respectively. $2N_f$ corresponds to the number of stress cycles to failure. This equation can be modified to take into account the effect of mean stress (σ_m) and is written as:

$$S_a = \left(S_f' - S_m\right)\left(2N_f\right)^b \quad (3)$$

Regression analysis of fatigue data for the SH specimens led to the relationship,

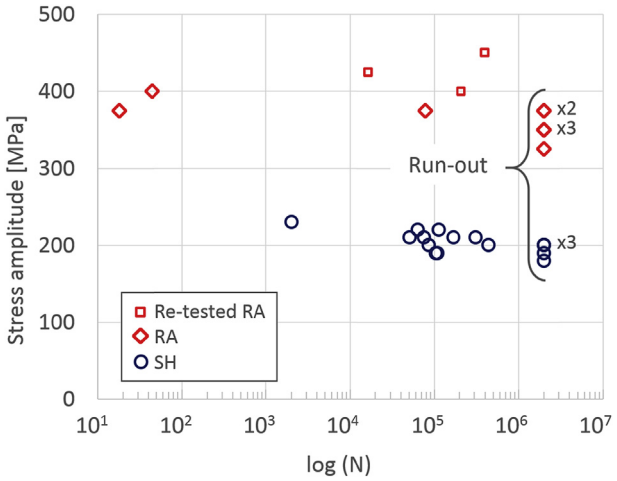

Fig. 8. S-N diagram for SH and RA specimens.

$$S_a = 376.94 \times \left(2N_f\right)^{-0.0501} \quad (4)$$

A similar relationship could not be derived for the RA specimens due to negligible plasticity and the relatively large experimental scatter involved. However, a one-sided confidence band could be calculated for the fatigue limit. Table 5 presents the mean fatigue limit and standard deviation for SH and RA specimens. Although the single specimen approach was effective in determining the initial stress-level for staircase testing, it should be preferably avoided. Specimen RA5 was initially tested at a stress-level corresponding to the fatigue ratio from previous results [4] and subsequently stepped up in relatively small increments until failure.

The replication rate of fatigue data is 62.50% for SH and 55.55% for RA. According to ASTM guidelines [25], SH specimens fall within the range of allowable data for design, whereas RA specimens are in the research and development regime.

Several specimens from the RA population were rejected due to failure at the grips. This problem had been previously observed for highly brittle, rolled tungsten specimens when using serrated wedge grips. In this study, it was found that the orientation of the specimen during mounting played a critical role; when gripped in the plane perpendicular to the rolling direction, the indentation from the wedge grips initiated cracks which propagated along the grain boundaries. In some cases, such a crack would travel along the entire grip surface, causing delamination. This issue was not as pronounced when the specimen was gripped in the same plane as the rolling direction. However, a number of specimens still failed and had to be rejected. In an attempt to avoid this problem, an aluminum sleeve was placed on the specimen head for protection from indentations. Unfortunately, this caused the specimens to glide in the sleeve at higher stresses. All the RA specimens showed grip damage to varying extents. An example of this is presented in the figures below (Fig. 9a–c). The SH material did not show any damage from such indentations, and no SH specimen was rejected. Additionally, there were no obvious signs of failure originating directly from the machining marks observed in the optical microscope prior to testing.

3.7. Strain-controlled fatigue experiments

In fully reversed straining at ±0.15% and a strain rate of 10^{-3} s^{-1}, the SH specimen showed rapid initial hardening for the first 20 cycles, as can be seen in Fig. 10 below. This was followed by a short

Table 4
Summary of staircase test data for SH and RA specimens.

Specimen	S_a [MPa]	S_{max} [MPa]	N_f (Cycles)	Specimen	S_a [MPa]	S_{max} [MPa]	N_f (Cycles)
SH4	180	365	Runout	RA5	325	655	Runout
SH5	230	465	2013	RA7	350	705	Runout
SH6	220	445	112514	RA9	375	755	18
SH7	210	425	170053	RA10	350	705	Runout
SH8	200	405	85874	RA11	375	755	Runout
SH9	190	385	108398	RA15	400	805	44
SH10	190	385	Runout	RA16	375	755	78020
SH11	200	405	Runout	RA18	350	705	Runout
SH12	210	425	75370	RA20	375	755	Runout
SH13	200	405	Runout				
SH14	210	425	310985				
SH15	200	405	Runout				
SH16	210	425	51097				
SH17	200	405	444943				
SH18	190	385	104094				
SH19	220	445	63725				

Table 5
Mean fatigue limit and standard deviation [MPa].

Material	S	σ
SH	185	26.4
RA	371	13.3

period of saturation and even marginal softening. After this, the specimen hardened gradually until failure after 90 cycles. Fig. 11 shows the stress response of the SH specimen during the first cycle in comparison with a cycle at saturation. The strength in tension, 400 MPa, during the first cycle is significantly lower than in compression, 490 MPa.

Since the RA specimens show very little plasticity, any strain controlled cyclic testing would result in a purely elastic response. The stress-strain response for cycle 1 and cycle 50, in the first step of multi-step testing of specimen RA17, show no significant differences. The completely elastic behavior can be seen in Fig. 12. The strain-controlled multiple-step test of specimen RA17, Fig. 13, shows a purely elastic response for all the steps until failure in step 4. Furthermore, the material is cyclically stable in each step and the observed changes in the stress range were negligible.

3.8. Fractography

The fracture surfaces of tungsten specimens were examined using a Scanning Electron Microscope (Philips XL 30 ESEM). It was observed that, in general, the SH specimens fractured predominantly in an intergranular manner. Larger grains showed a higher frequency of cleavage fracture, while smaller grains tended to remain intact.

SH specimens are associated with a porosity of about 4.3% and are likely to contain microcracks initiated at pores and inclusions. Catastrophic failure occurs due to the growth and coalescence of such microcracks [34] and as such, SH specimens should have a lower fatigue limit relative to RA specimens. The RA specimens tested in this work exhibited low ductility and anisotropic behavior.

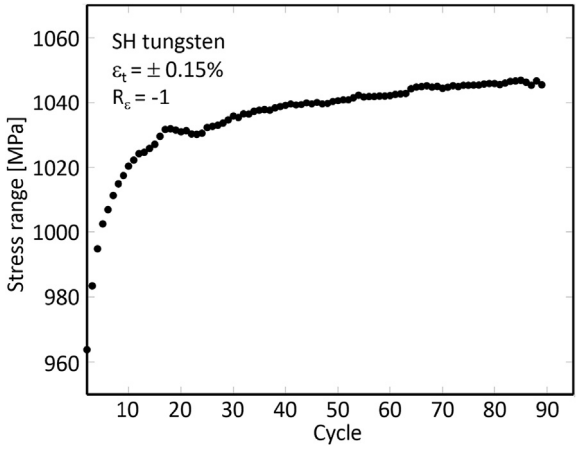

Fig. 10. Hardening of the SH specimen during a strain-controlled fatigue test.

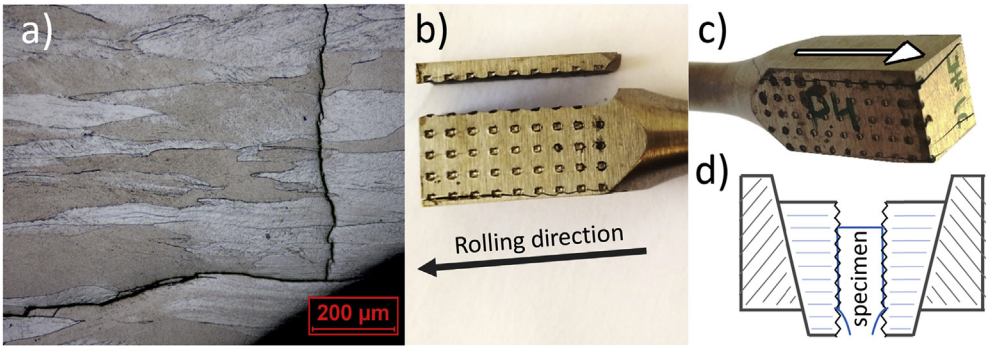

Fig. 9. a) A micrograph showing crack propagation in the RA specimen, initiated by grip indentations. Fig. 9b and c) shows large cracks and complete delamination, the arrows indicate the major rolling direction. Fig. 9d shows an illustration of the serrated wedge grips that are used in the fatigue and tensile tests.

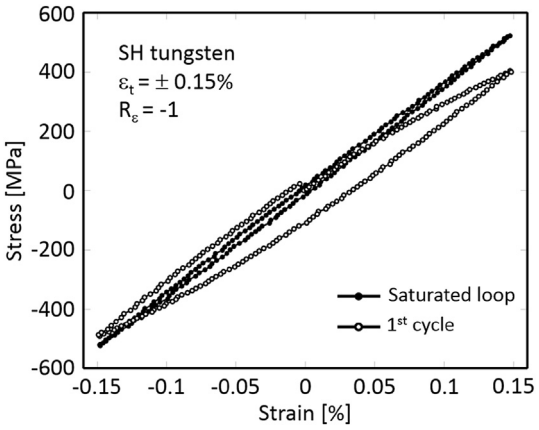

Fig. 11. Stress-Strain relationship during the initial and later stages of testing.

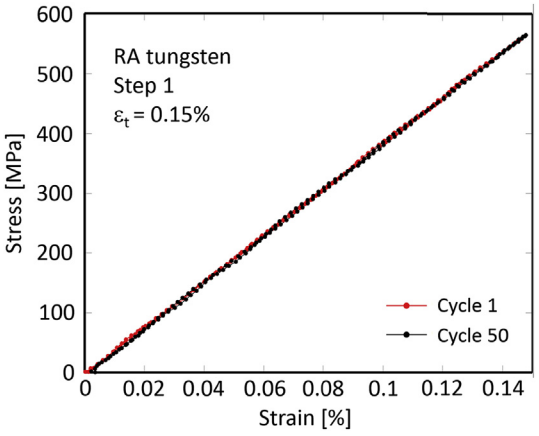

Fig. 12. The elastic response of specimen RA17 during the 1st and 50th cycle of step 1.

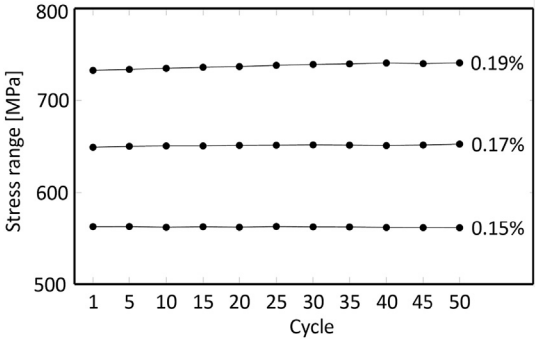

Fig. 13. The variation of stress with cyclic strain. The values at the end of each curve indicate the strain range at that step.

Typical SEM images of the fracture surfaces of SH and RA specimens are presented in Figs. 14–18.

All the RA specimens exhibited transcrystalline brittle failure. This behavior was observed both in the monotonic tensile test and fatigue samples. The large size of the grains (max. 1000 μm in length, with an aspect ratio of about 10) suggests that intergranular failures are unlikely. Further, the grains on the fracture surface do not show any sign of local deformation (Figs. 16 and 17). The transcrystalline nature of the failure in RA specimens can be clearly seen in these images.

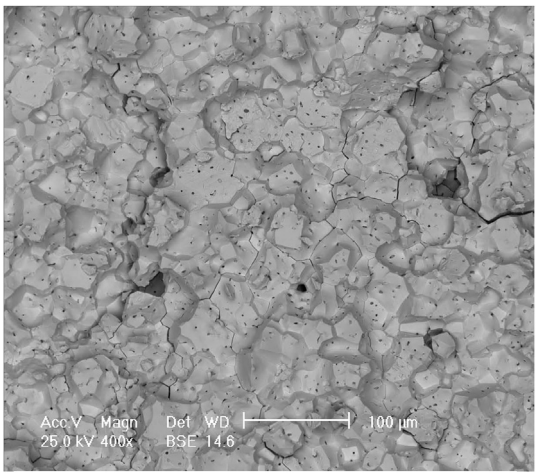

Fig. 14. Predominantly intergranular fracture in specimen SH14.

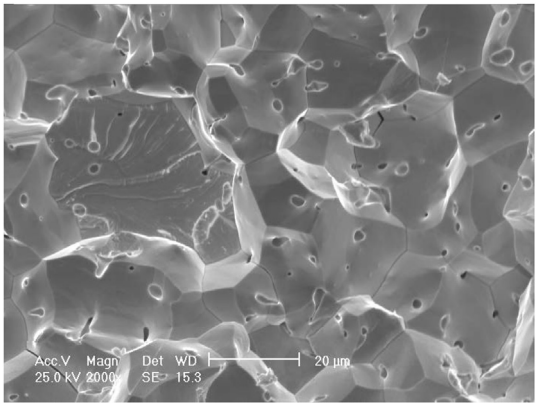

Fig. 15. Mixed inter- and transgranular failure in specimen SH2 after a tensile test.

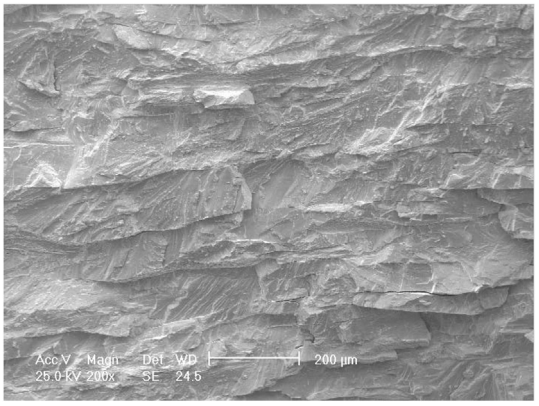

Fig. 16. SEM image of specimen RA10, showing transgranular cleavage.

The fracture surface shown in Fig. 18 suggests that the elongated grains contain subgrains and the specimen could fail through intergranular subgrain fracture.

3.9. Current work and target operating conditions

The stress amplitudes employed in the present work are much larger than the stress amplitudes induced by the beam pulse and

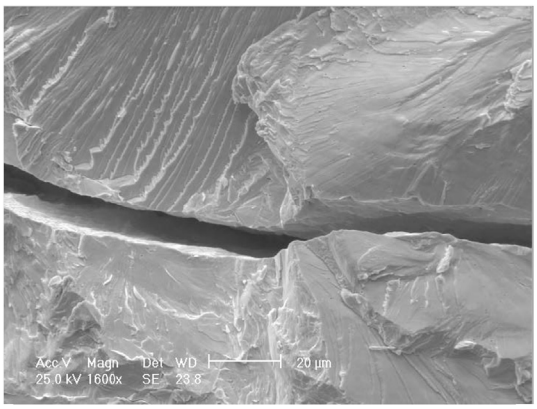

Fig. 17. Fracture surface showing river lines commonly observed in brittle failures.

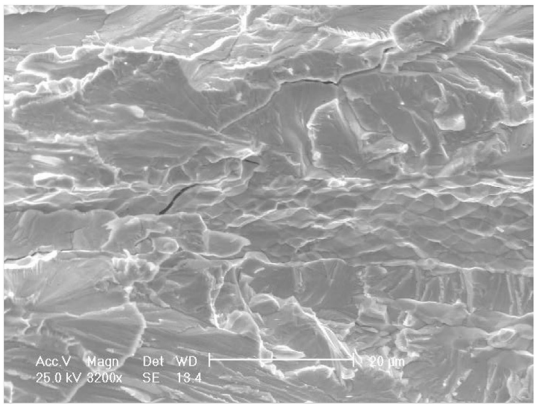

Fig. 18. SEM image of fracture surface of RA2, showing subgrains.

correspond better to the beam trips associated with stress amplitudes of about 110 MPa [1]. However, it has been reported in literature [17,35] that the ultimate tensile strength of an irradiated tungsten specimen could be as low as 60 MPa. Although the metallurgical condition of the tested material is not clearly stated in this paper, the low UTS value is a cause for concern while using pure tungsten targets. It may be noted that the tungsten target at ISIS operates at a maximum stress of 202 MPa [36], but is cladded with tantalum. The HIPing process used for cladding introduces compressive residual stresses in tantalum which help in holding the tungsten structure together. It has also been reported that tantalum retains its ductility up to a high irradiation dose [37].

4. Summary and conclusions

RA tungsten specimens used in this study were characterized by very large, elongated and flat interlocking grains (max. 1 mm long, aspect ratio ~10), a high tensile strength (998 MPa), and mean fatigue strength of 371 MPa.

Microstructural examination of the SH specimens showed grain size variation in the range 10–85 µm, with an average size of ~30 µm. Porosity in the specimens was ~4.3%, with most of the pores being relatively round (<5 μm^2) and evenly distributed in the material. The average UTS value was 567 MPa, while the mean fatigue strength was determined to be 185 MPa.

Microhardness measurements showed that RA specimens were much harder (508 VHN) than the SH specimens (389 VHN). Fractographic studies showed that SH tungsten fails in a predominantly intergranular manner and the monotonic tensile test specimens were found to have a slightly higher percentage of transgranular cleavage. On the other hand, RA specimens showed pure transgranular cleavage which could be attributed to the long and interlocking nature of the grains.

In strain-controlled tests at zero strain ratio, stress relaxation phenomenon was observed in the case of SH specimens. The relaxation in mean stress continued until no plastic strain was observed in a cycle. In fully reversed straining (±0.15%), there was a rapid initial hardening phase which was followed by a slower and gradual hardening of the specimen until failure.

Results from this work and literature data on irradiated tungsten present an important design guideline for the ESS target, which is to reduce the maximum tensile stress to a low level. The design requirement set for the tungsten blocks in the ESS target wheel is a maximum mean stress of 100 MPa, with a maximum stress amplitude of 50 MPa. The shape and size of the tungsten blocks has been chosen to meet these requirements. Simulations show that with the current design of the blocks ($8 \times 3 \times 1$ cm^3) the maximum mean stress will be below 100 MPa.

Acknowledgements

The authors are thankful to Zivorad Zivkovic for invaluable assistance in the experimental work. Research funding and support from the European Spallation Source (ESS, Lund) is gratefully acknowledged.

References

[1] A. Aguilar, M. Magan, I. Herranz, F. Sordo, T. Mora, R. Vivanco, G. Bakedano, J. Aguilar, L. Mena, M. Mancisidor, J.L. Martinez, Equipment Specification Document: Spallation Material, Report No. ESS-0058358, September 16, 2016.
[2] E. Abad, F. Sordo, Vibration Tests, Technical Report No. ESS-0055645, European Spallation Source ERIC, 2017.
[3] S. Peggs, R. Kreiser (Eds.), ESS Technical Design Report, April 2013, ISBN 978-91-980173-2-8.
[4] J. Habainy, S. Iyengar, Y. Lee, Y. Dai, Fatigue behavior of rolled and forged tungsten at 25°, 280° and 480°C, J. Nucl. Mater. 465 (2015) 438–447.
[5] A.S. Wronski, A.C. Chilton, The effects of temperature and pressurization on the tensile and compressive properties of polycrystalline cast tungsten, Scr. Metall. 3 (1969) 395–400.
[6] F.F. Schmidt, H.R. Ogden, DMIC Report 191: the Engineering Properties of Tungsten and Tungsten Alloys, 1963.
[7] D. Rupp, S.M. Weygand, Loading rate dependence of the fracture toughness of polycrystalline tungsten, J. Nucl. Mater. 417 (1–3) (2011) 477–480.
[8] V. Krsjak, S.H. Wei, S. Antusch, Y. Dai, Mechanical properties of tungsten in the transition temperature range, J. Nucl. Mater. 450 (1–3) (Jul. 2014) 81–87.
[9] P.L. Raffo, Yielding and fracture in tungsten and tungsten-rhenium alloys, J. Less-Common Met. 17 (1969) 133–149.
[10] H. Braun, K. Sedlatschek, On the influence of small additions of nonmetals and metals on the sintering, working and the mechanical properties of tungsten, J. Less-Common Met. 2 (1960) 277–291.
[11] K. Farrell, A.C. Schaffhauser, J.O. Stiegler, J. Less-Common Met. 13 (1967) 141–155.
[12] A. Giannattasio, S.G. Roberts, Strain-rate dependence of the brittle-to-ductile transition temperature in tungsten, Philos. Mag. 87 (17) (2007) 2589–2598.
[13] Y. Zhang, A.V. Ganeev, J.T. Wang, J.Q. Liu, I.V. Alexandrov, Observations on the ductile-to-brittle transition in ultrafine-grained tungsten of commercial purity, Mater. Sci. Eng. A 503 (1–2) (2009) 37–40.
[14] R.E. Schmunk, G.E. Korth, Tensile and low-cycle fatigue measurements on cross-rolled tungsten, J. Nucl. Mater. (1981) 943–948 vol. 103 & 104.
[15] B. Gludovatz, S. Wurster, T. Weingärtner, A. Hoffmann, R. Pippan, Influence of impurities on the fracture behaviour of tungsten, Philos. Mag. 91 (22) (2011) 3006–3020.
[16] T. Shen, Y. Dai, Y. Lee, Microstructure and tensile properties of tungsten at elevated temperatures, J. Nucl. Mater. 468 (2016) 348–354.
[17] I.V. Gorynin, V.A. Ignatov, V.V. Rybin, S.A. Fabritsiev, V.A. Kazakov, V.P. Chakin, V.A. Tsykanov, V.R. Barabash, Y.G. Prokofyev, Effects of neutron irradiation on properties of refractory metals, J. Nucl. Mater. 191–194 (1992) 421–425.
[18] ASTM E407: standard practice for microetching metals and alloys, in: Annual Book of ASTM Standards, vol. 3, 2007.
[19] ASTM E112–E113: Standard Test Methods for Determining Average Grain Size, ASTM International, West Conshohocken, PA, 2013.
[20] ASTM E8/E8M: standard test methods for tension testing of metallic materials 1, Annu. B. ASTM Stand. 4 (2010) 1–27 no. C.
[21] N.A. Fleck, C.S. Shin, R.A. Smith, Fatigue crack growth under compressive

loading, Eng. Fract. Mech. 21 (1) (1985) 173–185.
[22] W.J. Dixon, A.M. Mood, A method for obtaining and analyzing sensitivity data, J. Am. Stat. Assoc. 43 (241) (1948) 109–126.
[23] R. Pollak, A. Palazotto, T. Nicholas, A simulation-based investigation of the staircase method for fatigue strength testing, Mech. Mater. 38 (12) (2006) 1170–1181.
[24] K.A. Brownlee, J. Hodges Jr., M. Rosenblatt, The up-and-down method with small samples, J. Am. Stat. Assoc. 48 (262) (1953) 262–277.
[25] American Society for Metals, ASM Handb. Mech. Test. 8 (1985).
[26] N. Chawla, T. Murphy, K. Narasimhan, M. Koopman, K. Chawla, Axial fatigue behavior of binder-treated versus diffusion alloyed powder metallurgy steels, Mater Sci. Eng. A 308 (2001) 180–188.
[27] N. Chawla, X. Deng, Microstructure and mechanical behaviour of porous sintered steels, Mater Sci. Eng. A 390 (2005) 98–112.
[28] B. Gludovatz, S. Wurster, A. Hoffmann, R. Pippan, A study into the crack propagation resistance of pure tungsten, Eng. Fract. Mech. 100 (Mar. 2013) 76–85.
[29] C.L. Briant, E.L. Hall, The microstructure of rolled and annealed tungsten rod, Metall. Trans. A 20 (9) (1989) 1669–1686.
[30] M. Rieth, A. Hoffmann, Influence of microstructure and notch fabrication on impact bending properties of tungsten materials, Int. J. Refract. Met. Hard Mater. 28 (6) (2010) 679–686.
[31] D.T. Hurd, “Tungsten” in Metals Handbook, Volume 1, Properties and Selection of Metals, American Society for Metals, Metals Park, Novelty, Ohio, 1961.
[32] K.K. Phani, S.K. Niyogi, Young's modulus of porous brittle solids, J. Mater. Sci. 22 (1987) 257–263.
[33] S. Suresh, Fatigue of Materials, second ed., Cambridge University Press, Cambridge, 2004, pp. 223–226.
[34] G.S. Upadhyaya, Powder Metallurgy Technology, Cambridge International Science Publishing, Cambridge, 1997.
[35] H. Ullmaier, F. Carsughi, Radiation damage problems in high power spallation neutron sources, Nucl. Instrum. Methods Phys. Res. B 101 (1995) 406–421.
[36] P. Loveridge, D. Wilcox, Thermo-Mechanical Analysis of ISIS TS2 Spallation Target, 5th High Power Targetry Workshop, Fermilab, May 21, 2014.
[37] J. Chen, H. Ullmaier, T. Flossdorf, W. Kühnlein, R. Duwe, F. Carsughi, T. Broome, Mechanical properties of pure tantalum after 800 MeV proton irradiation, J. Nucl. Mater. 298 (2001) 248–254.